scientific reports

Check for updates

OPEN

Spin–orbit coupling in buckled monolayer nitrogene

Paulina Jureczko & Marcin Kurpas✉

Buckled monolayer nitrogene has been recently predicted to be stable above the room temperature. The low atomic number of nitrogen atom suggests, that spin–orbit coupling in nitrogene is weak, similar to graphene or silicene. We employ first principles calculations and perform a systematic study of the intrinsic and extrinsic spin–orbit coupling in this material. We calculate the spin mixing parameter b^2, reflecting the strength of the intrinsic spin–orbit coupling and find, that b^2 is relatively small, on the order of 10^{-6}. It also displays a weak anisotropy, opposite for electrons and holes. To study extrinsic effects of spin–orbit coupling we apply a transverse electric field enabling spin–orbit fields Ω. We find, that Ω are on the order of a single μeV in the valence band, and tens to a hundred of μeV in the conduction band, depending on the applied electric field. Similar to b^2, Ω is also anisotropic, in particular for the conduction electrons.

Two-dimensional (2D) pnictogens have gained a lot of attention in recent years[1–10]. Among these materials atomically thin black phosphorus emerged as the most promising one for electronic and spintronic applications due to its intrinsic semiconducting band gap, extraordinary high carrier mobility and strongly anisotropic orbital and spin properties[1,2,11,12]. Recently, 2D atomically thin nitrogen, called also *nitrogene*[13], has been predicted to be structurally stable even far above the room temperature[10,13,14]. According to these predictions, 2D nitrogene can crystallize in a few different forms, each having distinct electronic properties. Puckered (black phosphorus like) nitrogene is a direct gap semiconductor with the gap 1.25 eV[15]. Octagon nitrogene is an indirect wide-gap semiconductor with the gap 2.6 eV[16,17], while buckled honeycomb nitrogene is an indirect gap insulator with the calculated band gap of about 4–6 eV[13]. The wide band gap of buckled nitrogene may be an obstacle to use this material in semiconductor electronics. However, several ways of lowering the gap to the semiconducting limit have been proposed, including formation of multilayers[14], doping by boron[18] or making nitrogene nanoribbons[13].

So far the experimental realization of 2D nitrogene remains a challenge. The main obstacle here is a tendency of N atoms to form N_2 molecules with a triple N≡N bond[19]. Therefore, the goal is to find conditions under which this tendency is minimized, allowing for the formation of single bonds between N atoms. Such conditions can be created, for instance, by high pressure and temperature. Very recently this strategy has led to the synthesis of bulk nitrogen in black phosphorus structure[19,20]. More useful method, in terms of practical applications of nitrogene, was used by Harada et al., who epitaxially grown a single atom thick N layer in GaAs[21]. Although the structure of the epitaxial layer did not correspond to any of the theoretically envisaged, this is a big step towards the realization of 2D nitrogene.

Nitrogen is a light element with the atomic number Z=14. Therefore, spin–orbit coupling (SOC) in nitrogene is expected to be weak[22], similar to graphene[23] and phosphorene[12]. Indeed, in a recent theoretical study, Lee et al.[10] observed no significant effects of SOC on the band structure of buckled nitrognene. This may open great perspectives for this material in spintronics, since weak SOC should result in long lasting spin coherence. Buckled 2D nitrogene crystallizes in the centrosymmetric structure of the $P\bar{3}m1$ space group being isomorphic with the D_{3d} point group. The unit cell of nitrogene contains two nonequivalent atoms (Fig. 1b) belonging to two noncoplanar sublattices A and B. The finite out of plane buckling of the structure breaks the mirror symmetry of the lattice and allows the emergence of the *intrinsic Rashba*[24,25] spin–orbit coupling (PIA SOC in the context of functionalized graphene[26,27]). In contrast to the well known Bychkov–Rashba[28] SOC due to structure inversion asymmetry, the intrinsic Rashba SOC preserves the spin degeneracy of states, as a consequence of space inversion symmetry of the lattice and the time reversal symmetry. On the other hand, it affects the electron spin and leads to the emergence of in-plane spin components, forbidden by symmetry in flat, mirror symmetric graphene.

Besides the above general considerations, not much is known about SOC in this material. For instance, the question about the competition of the intrinsic Rashba SOC, polarizing the spins in-plane, and the intrinsic SOC polarizing spins along the z directions has not been addressed. Since such a competition may lead to the anisotropy of the SOC, we take up this problem here and perform a systematic study of SOC in buckled monolayer nitrogene. By employing first principles calculations we characterize the intrinsic SOC by the spin mixing

Institute of Physics, University of Silesia in Katowice, 41-500 Chorzów, Poland. ✉email: marcin.kurpas@us.edu.pl

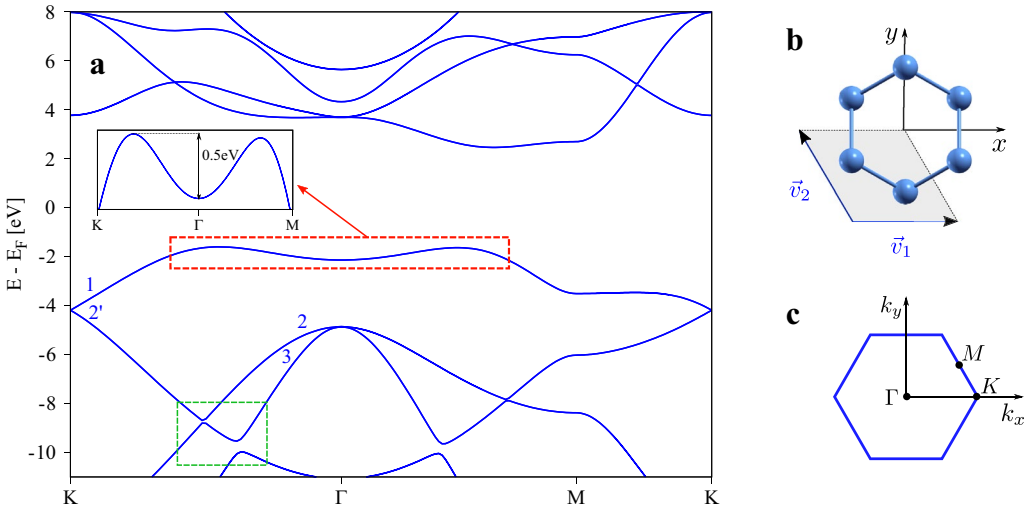

Figure 1. Electronic properties of monolayer nitrogene: (**a**) Calculated relativistic band structure of nitrogene plotted along high symmetry lines of the First Brillouin Zone shown in (**c**). The inset enlarges the valence band around the Γ point. The two maxima lie approximately 0.5 eV above the minimum at the Γ point; (**b**) crystalline structure of 2D nitrogene with the lattice vectors $\mathbf{v}_1$, $\mathbf{v}_2$, $|\mathbf{v}| = 0.69$ Å and the unit cell marked by the shaded area; (**c**) The First Brillouin Zone of 2D nitrogene with depicted high symmetry points.

parameter b^2[29], while the extrinsic SOC, arising due to breaking of the space inversion symmetry, is quantified by the amplitude of spin splittings Δ_{so} and spin–orbit fields Ω. All these quantities provide essential information about the strength and anisotropy of SOC in the band structure.

We find, that b^2 is of the order of 10^{-6}, both for electrons and holes, and displays a weak in-plane to out-of plane anisotropy. The extrinsic SOC shows significant diversity between the valence and conduction bands. In the former, the values of spin–orbit fields Ω vary between a few to a dozen of μeV for the considered amplitudes of an external electric field, and are rather isotropic. In the latter, the values of Ω are roughy ten times bigger and are strongly anisotropic.

Results and discussion

Intrinsic spin–orbit coupling. We begin our considerations from the examination of the electronic band structure of nitrogene. The calculated first principles relativistic band structure is shown in Fig. 1. Similar to other buckled 2D materials made of group V elements, such as blue phosphorene, arsenene or antimonene[22], the band gap of monolayer nitrogene is indirect. The size of the indirect gap for the PBE exchange correlation functional is $E_g = 4.06$, eV, and is in agreement with the values reported by others[13]. The top-most valence band has two local maxima lying between the ΓK and ΓM paths in the First Brillouin Zone (FBZ) (Fig. 1c). The maxima are located approximately 0.5 eV above the saddle point at the Γ point, and differ in energy by 35 meV. The edge of the conduction band is located in the middle of the ΓM path in the FBZ.

As already stated by Lee et al.[10], the effects of spin–orbit coupling on the band structure on buckled nitrogene are weak. Indeed, the inclusion of relativistic effects in the calculation makes no significant effects on the non-relativistic band structure. The most prominent ones are spin–orbital gaps opened at high symmetry points of the FBZ. In the valence band, the spin–orbital gap at the Γ point (between the bands marked 2 and 3) is $\Delta^{\Gamma}_{SO} = 17.3$ meV, while at the K point (between the bands marked 1 and 2') it is $\Delta^{K}_{SO} = 2.1$ meV. For comparison, the same splittings for graphene are $\Delta^{\Gamma}_{SO} = 9$ meV and $\Delta^{K}_{SO} = 24\ \mu$eV[23], and for blue phosphorene $\Delta^{\Gamma}_{SO} = 48$ meV, $\Delta^{K}_{SO} = 10\ \mu$eV[22].

To characterize the intrinsic SOC in the band structure away from the high symmetry points we calculate the spin mixing parameter b^2. This parameter measures the amplitude of the spin component being admixed to the Bloch state of opposite spin by the SOC. Importantly, the parameter b^2 can be easily accessed experimentally from the Elliott relation connecting b^2 with the spin τ_s and momentum τ_p relaxation times: $b^2 = \tau_p(4\tau_s)^{-1}$, provided the Elliott-Yafet mechanism dominates spin relaxation[29,30]. This is usually the case, when the spin lifetime follows the same characteristics as the momentum lifetime[31–34]. Knowing τ_p and τ_s from the experiment, one can extract the sample independent parameter b^2, and compare it with the theoretical values. Recently we have successfully applied this strategy to characterize b^2 and spin relaxation in black phosphorus[12,34]. In numerical simulations the parameter b^2 can be calculated directly from the wave functions, provided the spin subbands of a Bloch state $\psi_{\mathbf{k},n}$ are degenerate. This requirement is met if the time reversal symmetry and space inversion symmetry of the sample are present simultaneously. In such a case the two Bloch subbands are

$$\psi^{\Uparrow}_{\mathbf{k},n}(\mathbf{r}) = [a_{k,n}(\mathbf{r})|\uparrow\rangle + b_{k,n}(\mathbf{r})|\downarrow\rangle]e^{i\mathbf{k}\cdot\mathbf{r}}, \tag{1}$$

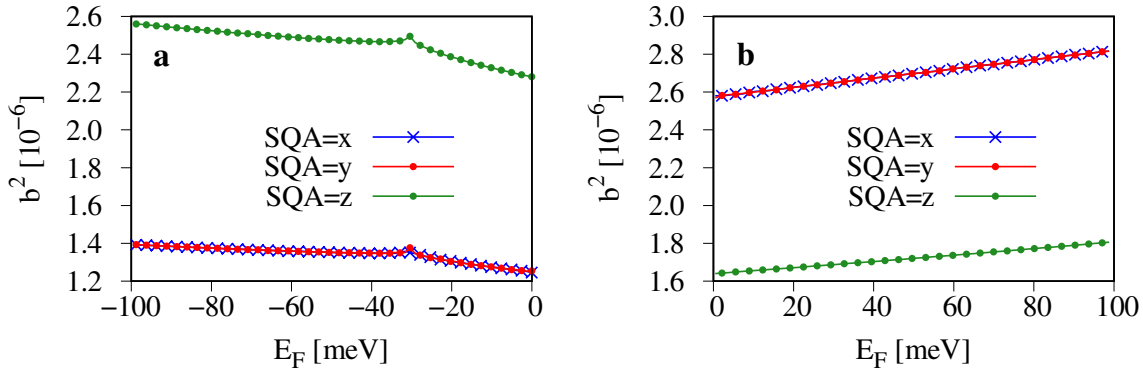

Figure 2. Calculated Fermi contour averaged spin-mixing parameter b^2 versus the position of the Fermi level E_F and for three directions of SQA aligned with the Cartesian system axes: (**a**) for the valence band; (**b**) for the conduction band. The Fermi level is measured with respect to the valence (conduction) band maximum (minimum).

$$\psi^{\Downarrow}_{\mathbf{k},n}(\mathbf{r}) = [a^{*}_{-k,n}(\mathbf{r})|\downarrow\rangle - b^{*}_{-k,n}(\mathbf{r})|\uparrow\rangle]e^{i\mathbf{k}\cdot\mathbf{r}}, \tag{2}$$

where n is the band index, $a_{k,n}$ and $b_{k,n}$ are lattice periodic functions, $\mathbf{k}$ is the crystal momentum and $|\uparrow\rangle, |\downarrow\rangle$ are eigenstates of the spin one-half operator with eigenvalues $\pm\hbar/2$[35]. Here, $b_{k,n}$ is the amplitude of spin component $|\sigma'\rangle$ being admixed by the SOC to the Bloch state of spin $|\sigma\rangle, \sigma = \{\uparrow, \downarrow\}$. Since the Bloch states $\psi^{\Uparrow}_{\mathbf{k},n}(\mathbf{r})$ and $\psi^{\Downarrow}_{\mathbf{k},n}(\mathbf{r})$ are degenerate at any k-point, any linear combination of these states is also an eigenstate of the Hamiltonian. This allows us to chose the amplitudes $a_{k,n}$ and $b_{k,n}$ in such a way, that $\psi^{\Uparrow}_{\mathbf{k},n}(\mathbf{r})$, $\psi^{\Downarrow}_{\mathbf{k},n}(\mathbf{r})$ diagonalize spin one-half operator $\hat{s}_i, i = x, y, z$. By doing so we can choose the spin quantization axis (SQA), SQA=i, which in experiment corresponds to the direction of magnetization of injected spins.

The spin mixing parameter can be calculated by integrating the amplitude $|b_{k,n,}|$ over the whole unit cell

$$b^2_{\mathbf{k},n} = \int |b_{\mathbf{k},n}(\mathbf{r})|^2 d^3\mathbf{r}, \tag{3}$$

or, alternatively by calculating the deviation of the expectation value of the spin operator $\hat{s}_i$ from its nominal value 1/2 (in units of $\hbar$)[36]

$$b^2_{\mathbf{k},n,i} = \frac{1}{2} - |\langle\psi^{\sigma,i}_{\mathbf{k},n}(\mathbf{r})|\hat{s}_i|\psi^{\sigma,i}_{\mathbf{k},n}(\mathbf{r})\rangle|, \tag{4}$$

where $\sigma = \{\Uparrow, \Downarrow\}$ and $\psi^{\sigma,i}_{\mathbf{k},n}(\mathbf{r})$ is the eigenstate of $\hat{s}_i$. For normalized states $0 \le b^2_{\mathbf{k},n,i} \le 0.5$, where $b^2_{\mathbf{k},n,i} = 0.5$ corresponds to fully spin mixed states and $b^2_{\mathbf{k},n,i} = 0$ to pure spin up (down) spinors.

The calculated Fermi contour averaged spin mixing parameter b^2 plotted versus the position of the Fermi level is shown in Fig. 2. The value of b^2 is in the range of 10^{-6} for both, the valence and the conduction band. This is roughly ten times the value of b^2 for graphene and ten times less than for black and blue phosphorus[22,34,37]. At $E_F \approx 32$ meV the second valence band maximum (along the ΓM path in Fig. 1) crosses the Fermi level and k-points from this wedge of the FBZ start contributing to b^2, slightly modifying its slope. The parameter b^2 is almost doping independent. Such behavior is typical for bands being energetically separated from other lower and higher lying bands[22].

The parameter b^2 shows weak anisotropy with respect to the spin quantization axis. In the valence band (Fig. 2a) b^2 for SQA=z (out of plane polarization) is roughly twice as large as for SQA=x, y, $b^2_{SQA=x/y}/b^2_{SQA=z} \approx 0.54$. This result is surprising, since most of buckled elemental monolayer materials display the opposite trend[22]. In this context nitrogene is similar to graphene, which exhibits similar anisotropy of b^2 for holes away from the Dirac point. For conduction electrons (Fig. 2b) we observe the opposite trend in b^2, namely, $b^2_{SQA=x/y}/b^2_{SQA=z} \approx 1.6$. Although the anisotropy of b^2 is not very high, this result deviates from other buckled pnictogens, for which b^2 is mostly isotropic.

The results presented Fig. 2 have been obtained for the PBE exchange–correlation functional. Since for hybrid functionals the band gap increases by 2 eV[13], we have checked how the band gap correction influences the values of the spin mixing parameter and performed calculations for the HSE[38] functional. Although the band gap increased to 6.34 eV (see Supplementary Fig. S1) the corresponding spin mixing parameter (Supplementary Fig. S2) stays almost unaffected and varies by at most a few percent. Therefore, the results obtained for the PBE functional can be taken as conclusive.

Extrinsic spin–orbit coupling. Monolayer nitrogene has been predicted to be structurally stable on metal surfaces. Even though the interaction with the substrate is weak and makes no significant changes to the band structure of nitrogene[13], the crystal potential at the interface breaks the inversion symmetry of the nitrogene lattice and enables the extrinsic Bychkov–Rashba spin–orbit coupling[28]. The extrinsic SOC has two main effects on the electron spin. First, it removes the degeneracy of spin states, and second, it induces crystal momentum

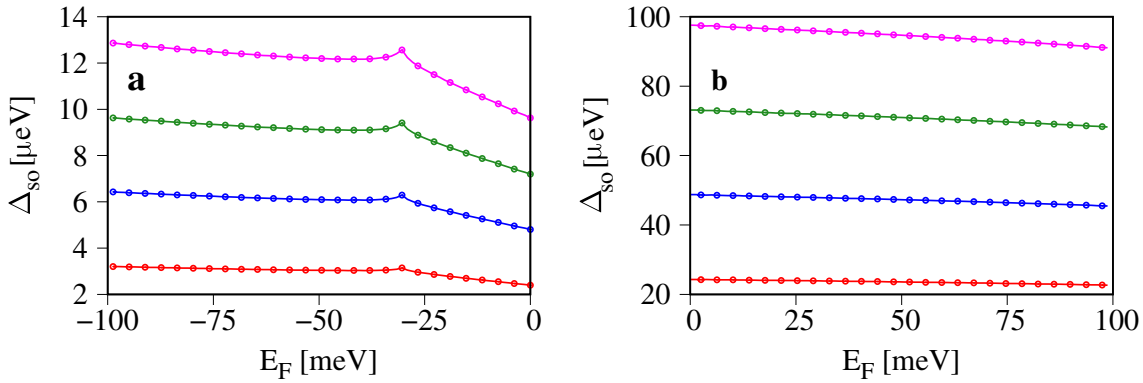

Figure 3. Fermi contour averaged spin splitting versus Fermi level for several values of the external electric field E, and for: (**a**) the top most valence band; (**b**) the bottom most conduction band. The Fermi level is measured with respect to the valence (conduction) band maximum (minimum).

dependent spin–orbital fields $\mathbf{\Omega}_k$, which lead to spin polarization of Bloch states and to the emergence of the characteristic spin texture in the FBZ. The SO field $\mathbf{\Omega}_k$ is linked to spin splitting by the Zeeman-like Rashba Hamiltonian

$$H_R(k) = \frac{\hbar}{2}\mathbf{\Omega}_k \cdot \boldsymbol{\sigma}, \tag{5}$$

where $\hbar$ is the Planck constant, and $\boldsymbol{\sigma}$ is the vector of Pauli matrices.

Instead of placing nitrogene on a particular substrate we model its presence by applying an external transverse electric field $\boldsymbol{E} = (0, 0, E)$, whose amplitude can be precisely controlled in numerical calculations. This approach, allowing us to simulate different substrates, is justified due to weak hybridization of states of nitrogene and the substrate[13].

In Fig. 3 we show the Fermi contour averaged spin splitting Δ_{so} calculated for several values of the electric field. In contrast to the spin mixing parameter b^2, Δ_{so} differs significantly between the valence and conduction band. In the former (Fig. 3a), Δ_{so} takes the values from a few to a dozen of μeV for the considered values of electric fields and grows by approximately 3 μeV per 1Vnm^{-1}. In the conduction band (Fig. 3b) the corresponding values are almost ten times bigger than in the valence band, and vary between 20 μeV to 100 μeV, for $E = 1$ Vnm^{-1} and $E = 4$ Vnm^{-1} respectively, with a linear growth of 33 μeV per 1 Vnm^{-1}. Similarly to b^2, the slope of Δ_{so} in the valence band changes slightly when the Fermi level $E_F \approx 32$ meV and the second valence band maximum (between the Γ and M points in Fig. 1) enters the Fermi contour.

The spin splitting Δ_{so} characterizes the strength of the extrinsic SOC in a band. The anisotropy of SOC can be accessed through the components of the spin–orbit field $\mathbf{\Omega}_k$, $\Omega_{k,i}$,

$$\Omega_{k,i} = \frac{\Delta_{so}(k)}{\hbar}\frac{S_{k,i}}{S_k}, \tag{6}$$

where S_i, $i = \{x, y, z\}$ is the expectation value of spin one-half operator at a given k point, and $S_k = \sqrt{S_{k,x}^2 + S_{k,y}^2 + S_{k,z}^2}$ [39]. The calculated Fermi surface averaged components Ω_i are presented in Fig. 4. In the valence band (Fig. 4a,b), Ω_x and Ω_y take similar values, while Ω_z (Fig. 4c) is almost twice smaller and displays different monotonicity. In the conduction band, the in-plane spin components Ω_x, Ω_y (Fig. 4d,e) are large, tens of μeV, and are doping independent, while Ω_z (Fig. 4f) takes the values of a few μeV, and is doping dependent. Such big differences between $\Omega_{x/y}$ and Ω_z lead to a sizeable, up to $\Omega_{x/y}/\Omega_z \approx 40$, doping-dependent anisotropy.

To understand these results one needs to look at the components of the electron spin which shape Ω_i. We show them in Fig. 5a,b. The in-plane spin components S_x and S_y form the typical circulating Rashba spin texture (Fig. 5a). Within the considered doping range the length of S_x and S_y is approximately constant, as shown in Fig. 5c. The S_z component displays much bigger diversity, and takes small values in the center of FBZ, while for bigger crystal momenta we observe the spin-valley locking effect with a strong spin polarization. In effect, when doping increases the average value of $|S_z|$ in the valence band first decreases from the value $|S_z| \approx 0.1$ to $|S_z| \approx 0.03$, and for $E_F \leq -32$ meV its starts increasing and saturates at the value $|S_z| \approx 0.075$ (Fig. 5c). The qualitative change to S_z takes place when the Fermi contour reaches the k-points close to the anticrossings marked by the green rectangle in Fig. 1a, what happens exactly at $E_F \approx -32$ meV. For k in the range from the Γ point to the anticrossing at $E - E_F \approx -10$ eV, $S_z \approx 0$ (see the Supplementary Fig. S3). Increasing k towards the K-point, S_z starts growing and reaches the maximum $S_z \approx 0.5$ at k above the anticrossing lying at $E - E_F \approx -9$ eV. Since the valence band maximum lies in between of the two anticrossings, we first observe a decrease of $|S_z|$ followed by its increase.

In the conduction band (Fig. 5b,d), the in-plane spins also form the Rashba texture, similar to the valence band, but the z component of spin is very small in the wedge of the BZ corresponding to doping range

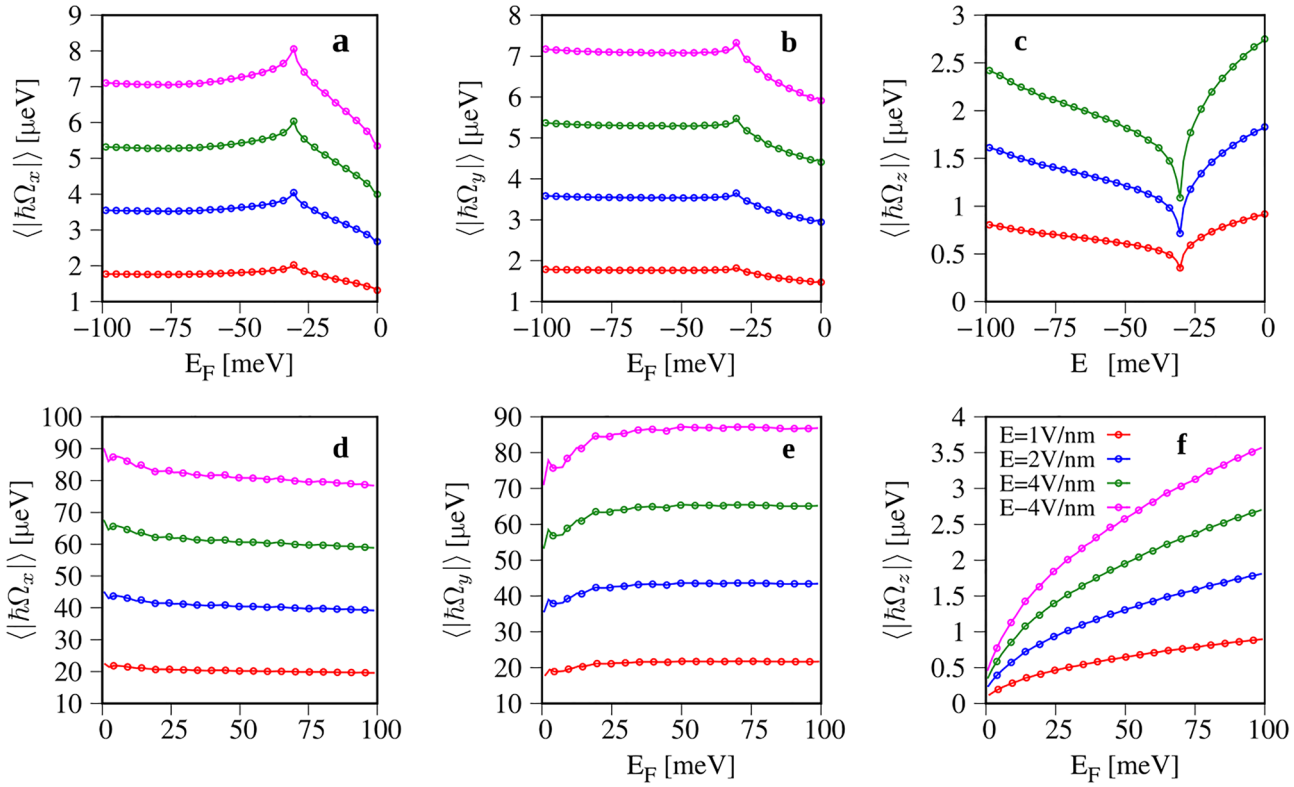

Figure 4. Fermi contour averaged components of the spin–orbit field $\hbar\Omega$ versus the position of Fermi level E_F and for several values of electric field E. Panels (**a**–**c**) show the x, y, and z components of $\mathbf{\Omega}$ for the valence band respectively; (**d**–**f**), same as (**a**–**c**) but for the conduction band. The Fermi energy is measured with respect to the valence (conduction) band maximum (minimum).

(represented by black ellipses). In effect, Ω_x and Ω_y take the values close to Δ_{so}, while Ω_z is of the order of a few μeV (Fig. 4d–f), generating a large anisotropy of the extrinsic SOC.

As can be seen from the results shown above, SOC in nitrogene is weak. The calculated spin mixing parameter, $b^2 \approx 10^{-6}$, is approximately ten times bigger than for graphene[22]. This suggests, that the intrinsic SOC should not contribute much to spin scattering in nitrogene. Taking the typical momentum lifetime $\tau_p = 100$ fs, we can make a rough estimate of spin lifetime from the Elliott-Yafet mechanism[29,31],$\tau_s^{EY} \approx \tau_p/4b^2 \approx 50$ ns. On the other hand, several factors may affect SOC and spin dynamics in a material. For instance in graphene, the out-of-plane lattice distortions strongly affect both, the strength of the SOC and momentum scattering, dramatically reducing spin lifetime[40–43]. A transition from the flat to rippled graphene results in the emergence of an additional (intrinsic) SO term H_{curv}[42,44]. For typical ripples of radii in the range $R \sim 50$ nm-100 nm the characteristic energy of this interaction is $\Delta_{curv} \approx 0.2$ K, and can exceed the energy of the intrinsic SOC, $\Delta_{int} \approx 0.01$ K $-$ 0.1 K[23,42], making the relevant spin-flip processes important. Additionally, rippling breaks the mirror symmetry ($z \to -z$) protecting the electron spin, and enables additional spin relaxation channels by flexural phonons and random spin–orbit fields[41,43].

In contrast to graphene, nitrogene is naturally buckled. Thus, the effects of buckling are embedded in the intrinsic SOC and b^2, and are much stronger than effects of rippling discussed above. It was shown, that Δ_{int} at the K-point in graphene grows quadratically with the buckling height δ, $\Delta_{int} \sim (\delta/a)^2$, a being the lattice constant, and for $\delta/a \approx 0.08$ it jumps to $\Delta_{int} \approx 1$ K[23]. In the case of nitrogene, the buckling height is $\delta \approx 0.9$Å, $a = 2.3$ Å, which gives $\delta/a \approx 0.4$. Following the quadratic dependence for graphene, one gets for nitrogene $\Delta_{int} = 25$ K, close to the value $\Delta_{so}^K = 23$ K extracted from our first principles calculations. For comparison, static ripples of radii $R \sim 50$ nm-100 nm, give the correction to the intrinsic SOC of the order of $\Delta_{curv} \sim a/R \approx 0.2$ K[42],—negligible in the case of nitrogene.

Although lattice ripples should not significantly affect the intrinsic SOC in nitrogene, they can generate a small random spin–orbit fields leading to faster spin decoherence, in a similar way as it takes place graphene[41]. Fortunately, lattice rippling can be to a large extent eliminated by encapsulation of the host layer by, e.g., hexagonal boron nitride[45,46].

spin–orbit coupling plays an important role in contemporary solid state physics, spintronics and topological quantum computing. Apart from these areas of physics, it has also been intensively studied in cold atoms systems. Therefore, in the next few lines we briefly compare SOC in crystalline solids with SOC in Bose gases.

In crystalline solids, SOC originates from the crystal potential, in which an electron is moving. In the rest frame of the electron, the electric field induced by the crystal potential acts as an effective, momentum dependent Zeeman field acting on the electron spin. The strength of SOC in a band is determined by the chemical

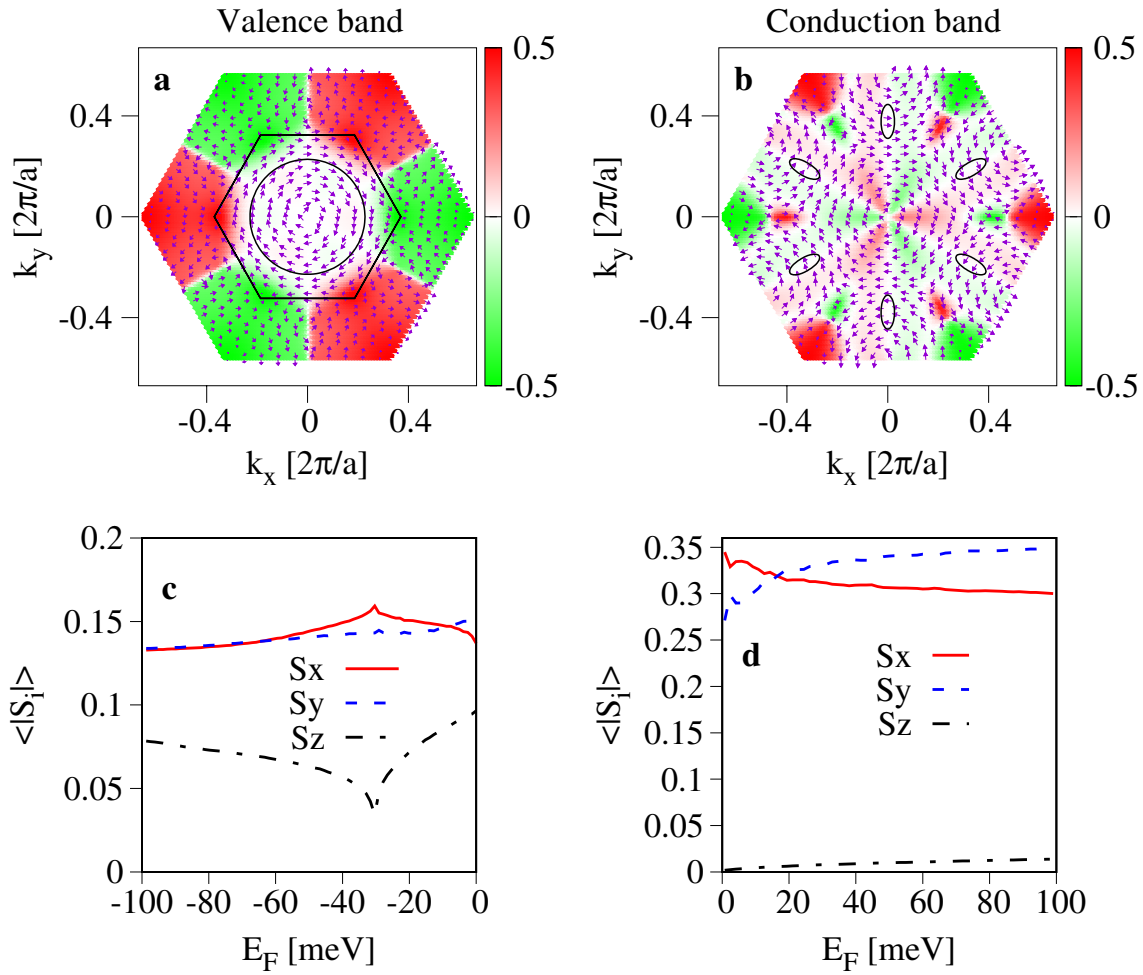

Figure 5. Effects of the extrinsic SOC on the electron spin: (**a**) the induced in-plane spin texture (arrows) and s_z component of spin (color) for the top-most valence band and the electric field $E = 1$ Vnm; (**c**) The corresponding Fermi surface averaged spin expectation values versus doping. The BZ wedge corresponding to doping in the range 0–100 meV is given by the area limited by the black hexagon and circle; (**b**,**d**) same as (**a**,**c**) but for the conduction band.

composition of the crystal (materials made of heavier elements display stronger SOC effects than those made of light elements) and the topology of the band structure, and to some extent may be modified externally, e.g., by electric fields[47], strain[48], proximity effects[49] or twisting[50]. The form of the spin–orbit interaction is dictated by the symmetry of the crystal; for instance, the famous Bychkov–Rashba[28] and Dresselhaus[51] types of SOC result from broken structure and bulk inversion symmetry, respectively.

In cold bosons systems, SOC is realized by coupling the motion of an atom to its internal (hyperfine) pesudo-spin states, corresponding to the electron's spin *up* and spin *down* states[52–56]. Implementation of such coupling, called *synthetic* SOC[54], requires an extra effort of dressing atomic states with lasers, but offers a full control of this interaction at will[57]. By a proper combination of laser fields and atomic pseudo-spin states, a variety of SOCs can be created and dynamically modified[54,57,58]. For example, Lin et al.[54], realized one dimensional SOC, corresponding to equal contributions of Bychkov–Rashba and Dresselhaus SOC in conventional systems; Wu et al.[57] implemented a scheme allowing for a controllable transition from 1D to 2D SOC. More exotic forms of SOC having no counterparts in real materials, such as, a 3D analogue of Rashba SOC[59,60], are also possible, making cold atoms systems a powerful platform for exploring spin–orbit coupling and many body physics. Like in conventional materials, in bose gases, SOC is essential to the emergence of fascinating physical phenomena, e.g., a degenerate ground state of spin–orbit coupled Bose–Einstein condensates[61], spatial separation of BEC[54,62,63], quantum phase transitions[64], or the existence of topologically non-trivial phases[57,60]. These few examples are a small sample of SOC-induced phenomena in cold atoms systems. A more detailed discussion of this topic can be found in Refs.[65–69].

Conclusions

We have investigated the fundamental spin–orbit coupling in buckled monolayer nitrogene. Based on first principles calculations we found that spin mixing parameter characterising the intrinsic SOC is small, on the order of $b^2 \approx 10^{-6}$, and displays weak anisotropy. The extrinsic SOC, characterized by the Rashba spin–orbit fields Ω, is also weak, on the order of μeV in the valence and tens to a hundred of μeV in the conduction band. Similar to the intrinsic SOC, the extrinsic SOC is also anisotropic. The anisotropy is particularly strong in the conduction band. Weak spin–orbit coupling in nitrogene suggests, that doped nitrogene or nitrogene nanoribbons may be attractive materials for spintronics applications.

Methods

First-principles calculations were performed with the Quantum Espresso package[70,71]. The norm-conserving pseudopotential with the Perdew–Burke–Ernzerhof (PBE)[72,73] version of the generalized gradient approximation (GGA) exchange-correlation functional was chosen, taking the kinetic energy cutoff of the plane-wave basis 80 Ry for the wave function and 320 Ry for charge density respectively. These parameters were found to give well converged results. Calculations with a hybrid functional were done with the Heyd–Scuseria–Ernzerhof (HSE06)[38] functional, with the Fock exchange contribution 20%. Monolayer nitrogene was placed in a vacuum of 21 Å to minimize interactions between periodic copies of the system. Self-consistency was achieved with $21k_x \times 21k_y \times 1k_z$ Monkhorst-Pack grid[74]. The optimized lattice constant a was determined by minimizing the total energy followed by fitting a parabolic function. In each step the positions of atoms were fully relaxed by the quasi-Newton scheme as implemented in Quantum Espresso, assuming force convergence threshold 10^{-4} Ry/bohr. We found $a = 2.29$ Å and the out of plane buckling of the lattice $\delta = 0.96$ Å, similar to those reported by other authors[13]. Calculations with the electric field were carried out with the dipole correction[75]. Fermi contour averages of spin mixing parameter b^2, spin–orbit field Ω^2 and spin components s_i were calculated according to the formula

$$\langle A \rangle = \frac{1}{\rho(E_F) S_{BZ}} \int_{FC} \frac{A_k}{\hbar |\boldsymbol{v}_F(k)|} dk, \tag{7}$$

where A_k stands for b_k^2, Ω_k^2 and $s_{k,i}$, S_{BZ} is the area of the Fermi surface, $\rho(E_F)$ is the density of states per spin at the Fermi level, $\boldsymbol{v}_F(k)$ is the Fermi velocity.

Received: 22 November 2021; Accepted: 7 February 2022
Published online: 25 February 2022

References

1. Liu, H. *et al.* Phosphorene: An unexplored 2d semiconductor with a high hole mobility. *ACS Nano* **8**, 4033–4041. https://doi.org/10.1021/nn501226z (2014) (**PMID: 24655084**).
2. Xia, F., Wang, H. & Jia, Y. Rediscovering black phosphorus as an anisotropic layered material for optoelectronics and electronics. *Nat. Commun.* **5**, 4458. https://doi.org/10.1038/ncomms5458 (2014).
3. Castellanos-Gomez, A. *et al.* Isolation and characterization of few-layer black phosphorus. *2D Mater.* **1**, 025001. https://doi.org/10.1088/2053-1583/1/2/025001 (2014).
4. Zhu, Z., Guan, J. & Tománek, D. Strain-induced metal-semiconductor transition in monolayers and bilayers of gray arsenic: A computational study. *Phys. Rev. B* **91**, 161404. https://doi.org/10.1103/PhysRevB.91.161404 (2015).
5. Zhang, S., Yan, A., Li, Y., Chen, Z. & Zeng, H. Atomically thin arsenene and antimonene: Semimetal-semiconductor and indirect-direct band-gap transitions. *Angew. Chem.* **54**, 3112. https://doi.org/10.1002/anie.201411246 (2015).
6. Kamal, C. & Ezawa, M. Arsenene: Two-dimensional buckled and puckered honeycomb arsenic systems. *Phys. Rev. B* **91**, 085423. https://doi.org/10.1103/PhysRevB.91.085423 (2015).
7. Reis, F. *et al.* Bismuthene on a SiC substrate: A candidate for a high-temperature quantum spin Hall material. *Science* **357**, 287. https://doi.org/10.1126/science.aai8142 (2017).
8. Zhang, W. *et al.* Epitaxial synthesis of blue phosphorene. *Small* **14**, 1804066. https://doi.org/10.1002/smll.201804066 (2018).
9. Ersan, F. *et al.* Two-dimensional pnictogens: A review of recent progresses and future research directions. *Appl. Phys. Rev.* **6**, 021308. https://doi.org/10.1063/1.5074087 (2019).
10. Lee, J., Tian, W.-C., Wang, W. & Yao, D.-X. Two-dimensional pnictogen honeycomb lattice: Structure, on-site spin–orbit coupling and spin polarization. *Sci. Rep.* **5**, 11512. https://doi.org/10.1038/srep11512 (2015).
11. Liang, L. *et al.* Electronic bandgap and edge reconstruction in phosphorene materials. *Nano Lett.* **14**, 6400–6406. https://doi.org/10.1021/nl502892t (2014) (**PMID: 25343376**).
12. Kurpas, M., Gmitra, M. & Fabian, J. Spin–orbit coupling and spin relaxation in phosphorene: Intrinsic versus extrinsic effects. *Phys. Rev. B*https://doi.org/10.1103/PhysRevB.94.155423 *(2016).*
13. Özçelik, V. O., Aktürk, O. U., Durgun, E. & Ciraci, S. Prediction of a two-dimensional crystalline structure of nitrogen atoms. *Phys. Rev. B* **92**, 125420. https://doi.org/10.1103/PhysRevB.92.125420 (2015).
14. Lee, J., Wang, W. & Yao, D.-X. Band gap engineering of two-dimensional nitrogene. *Sci. Rep.*https://doi.org/10.1038/srep34177 *(2016).*
15. Bondarchuk, S. V. & Minaev, B. F. Two-dimensional honeycomb (A7) and zigzag sheet (ZS) type nitrogen monolayers. A first principles study of structural, electronic, spectral, and mechanical properties. *Comput. Mater. Sci.* **133**, 122–129. https://doi.org/10.1016/j.commatsci.2017.03.007 (2017).
16. Zhang, Y., Lee, J., Wang, W.-L. & Yao, D.-X. Two-dimensional octagon-structure monolayer of nitrogen group elements and the related nano-structures. *Comput. Mater. Sci.* **110**, 109–114. https://doi.org/10.1016/j.commatsci.2015.08.008 (2015).
17. Lin, W., Li, J., Wang, W., Liang, S.-D. & Yao, D.-X. Electronic structure and band gap engineering of two-dimensional octagon-nitrogene. *Sci. Rep.*https://doi.org/10.1038/s41598-018-19496-7 *(2018).*
18. Hoat, D. *et al.* Engineering the electronic and magnetic properties of nitrogene monolayer and bilayer by doping: A first-principles study. *Appl. Surf. Sci.* **566**, 150711. https://doi.org/10.1016/j.apsusc.2021.150711 (2021).
19. Ji, C. *et al.* Nitrogen in black phosphorus structure. *Sci. Adv.* **6**, eaba9206. https://doi.org/10.1126/sciadv.aba9206 (2020).

20. Laniel, D. *et al.* High-pressure polymeric nitrogen allotrope with the black phosphorus structure. *Phys. Rev. Lett.* **124**, 216001. https://doi.org/10.1103/PhysRevLett.124.216001 (2020).
21. Harada, Y., Yamamoto, M., Baba, T. & Kita, T. Epitaxial two-dimensional nitrogen atomic sheet in GaAs. *Appl. Phys. Lett.* **104**, 1–5. https://doi.org/10.1063/1.4863442 (2014).
22. Kurpas, M., Junior, P. E. F., Gmitra, M. & Fabian, J. Spin–orbit coupling in elemental two-dimensional materials. *Phys. Rev. B* **100**, 125422. https://doi.org/10.1103/PhysRevB.100.125422 (2019).
23. Gmitra, M., Konschuh, S., Ertler, C., Ambrosch-Draxl, C. & Fabian, J. Band-structure topologies of graphene: Spin–orbit coupling effects from first principles. *Phys. Rev. B* **80**, 235431. https://doi.org/10.1103/PhysRevB.80.235431 (2009).
24. Liu, C.-C., Jiang, H. & Yao, Y. Low-energy effective Hamiltonian involving spin–orbit coupling in silicene and two-dimensional germanium and tin. *Phys. Rev. B* **84**, 195430. https://doi.org/10.1103/PhysRevB.84.195430 (2011).
25. Geissler, F., Budich, J. C. & Trauzettel, B. Group theoretical and topological analysis of the quantum spin Hall effect in silicene. *New J. Phys.* **15**, 085030. https://doi.org/10.1088/1367-2630/15/8/085030 (2013).
26. Gmitra, M., Kochan, D. & Fabian, J. Spin–orbit coupling in hydrogenated graphene. *Phys. Rev. Lett.* **110**, 246602. https://doi.org/10.1103/PhysRevLett.110.246602 (2013).
27. Kochan, D., Irmer, S. & Fabian, J. Model spin–orbit coupling hamiltonians for graphene systems. *Phys. Rev. B* **95**, 165415. https://doi.org/10.1103/PhysRevB.95.165415 (2017).
28. Bychkov, Y. A. & Rashba, É. I. Properties of a 2D electron gas with lifted spectral degeneracy. *Sov. J. Exp. Theor. Phys. Lett.* **39**, 78 (1984).
29. Elliott, R. J. Theory of the effect of spin–orbit coupling on magnetic resonance in some semiconductors. *Phys. Rev.* **96**, 266–279. https://doi.org/10.1103/PhysRev.96.266 (1954).
30. Fabian, J. & Das Sarma, S. Spin relaxation of conduction electrons in polyvalent metals: Theory and a realistic calculation. *Phys. Rev. Lett.* **81**, 5624–5627. https://doi.org/10.1103/PhysRevLett.81.5624 (1998).
31. Yafet, Y. In *Solid State Physics* (eds Seitz, F. & Turnbull, D.) (Academic,1963).
32. Monod, P. & Beuneu, F. Conduction-electron spin flip by phonons in metals: Analysis of experimental data. *Phys. Rev. B* **19**, 911–916. https://doi.org/10.1103/PhysRevB.19.911 (1979).
33. Žutić, I., Fabian, J. & Das Sarma, S. Spintronics: Fundamentals and applications. *Rev. Mod. Phys.* **76**, 323. https://doi.org/10.1103/RevModPhys.76.323 (2004).
34. Avsar, A. *et al.* Gate-tunable black phosphorus spin valve with nanosecond spin lifetimes. *Nat. Phys.* **13**, 888. https://doi.org/10.1038/nphys4141 (2017).
35. Zimmermann, B. *et al.* Anisotropy of spin relaxation in metals. *Phys. Rev. Lett.* **109**, 236603. https://doi.org/10.1103/PhysRevLett.109.236603 (2012).
36. Zimmermann, B. *et al.* Fermi surfaces, spin-mixing parameter, and colossal anisotropy of spin relaxation in transition metals from ab initio theory. *Phys. Rev. B* **93**, 144403. https://doi.org/10.1103/PhysRevB.93.144403 (2016).
37. Kurpas, M., Gmitra, M. & Fabian, J. Spin properties of black phosphorus and phosphorene, and their prospects for spincalorics. *J. Phys. D. Appl. Phys.*https://doi.org/10.1088/1361-6463/aab5a2 *(2018).*
38. Heyd, J., Scuseria, G. E. & Ernzerhof, M. Hybrid functionals based on a screened coulomb potential. *J. Chem. Phys.* **118**, 8207–8215. https://doi.org/10.1063/1.1564060 (2003).
39. Fabian, J., Matos-Abiague, A., Ertler, C., Stano, P. & Žutić, I. Semiconductor spintronics. *Acta Phys. Slov. Rev. Tutor.*https://doi.org/10.2478/v10155-010-0086-8 *(2007).*
40. Castro, E. V. *et al.* Limits on charge carrier mobility in suspended graphene due to flexural phonons. *Phys. Rev. Lett.* **105**, 266601. https://doi.org/10.1103/PhysRevLett.105.266601 (2010).
41. Dugaev, V. K., Sherman, E. Y. & Barnaś, J. Spin dephasing and pumping in graphene due to random spin–orbit interaction. *Phys. Rev. B* **83**, 1–8. https://doi.org/10.1103/PhysRevB.83.085306 (2011).
42. Huertas-Hernando, D., Guinea, F. & Brataas, A. Spin–orbit coupling in curved graphene, fullerenes, nanotubes, and nanotube caps. *Phys. Rev. B*https://doi.org/10.1103/PhysRevB.74.155426 *(2006).*
43. Vicent, I. M., Ochoa, H. & Guinea, F. Spin relaxation in corrugated graphene. *Phys. Rev. B*https://doi.org/10.1103/PhysRevB.95.195402 *(2017).*
44. Ando, T. Spin–orbit interaction in carbon nanotubes. *J. Phys. Soc. Jpn.* **69**, 1757–1763. https://doi.org/10.1143/JPSJ.69.1757 (2000).
45. Ingla-Aynés, J., Guimarães, M. H. D., Meijerink, R. J., Zomer, P. J. & van Wees, B. J. 24 $-$ μm spin relaxation length in boron nitride encapsulated bilayer graphene. *Phys. Rev. B* **92**, 201410. https://doi.org/10.1103/PhysRevB.92.201410 (2015).
46. Drögeler, M. *et al.* Spin lifetimes exceeding 12 ns in graphene nonlocal spin valve devices. *Nano Lett.* **16**, 3533–3539. https://doi.org/10.1021/acs.nanolett.6b00497 (2016).
47. Premasiri, K. *et al.* Tuning Rashba spin–orbit coupling in gated multilayer InSe. *Nano Lett.* **18**, 4403–4408. https://doi.org/10.1021/acs.nanolett.8b01462 (2018).
48. Fülöp, B. *et al.* Boosting proximity spin–orbit coupling in graphene/WSe2 heterostructures via hydrostatic pressure. *NPJ 2D Mater. Appl.* **5**, 82. https://doi.org/10.1038/s41699-021-00262-9 (2021).
49. Avsar, A. *et al.* Spin–orbit proximity effect in graphene. *Nat. Commun.***5**, 4875, https://doi.org/10.1038/ncomms5875 (2014). arXiv:9809069.
50. David, A., Rakyta, P., Kormányos, A. & Burkard, G. Induced spin–orbit coupling in twisted graphene-transition metal dichalcogenide heterobilayers: Twistronics meets spintronics. *Phys. Rev. B* **100**, 085412. https://doi.org/10.1103/PhysRevB.100.085412 (2019).
51. Dresselhaus, G. Spin–orbit coupling effects in zinc blende structures. *Phys. Rev.* **100**, 580–586. https://doi.org/10.1103/PhysRev.100.580 (1955).
52. Higbie, J. & Stamper-Kurn, D. M. Periodically dressed Bose–Einstein condensate: A superfluid with an anisotropic and variable critical velocity. *Phys. Rev. Lett.* **88**, 090401. https://doi.org/10.1103/PhysRevLett.88.090401 (2002).
53. Osterloh, K., Baig, M., Santos, L., Zoller, P. & Lewenstein, M. Cold atoms in non-abelian gauge potentials: From the hofstadter "moth" to lattice gauge theory. *Phys. Rev. Lett.* **95**, 1–4. https://doi.org/10.1103/PhysRevLett.95.010403 (2005).
54. Lin, Y.-J., Jiménez-García, K. & Spielman, I. B. Spin–orbit-coupled Bose–Einstein condensates. *Nature* **471**, 83–86. https://doi.org/10.1038/nature09887 (2011).
55. Fu, Z., Wang, P., Chai, S., Huang, L. & Zhang, J. Bose–Einstein condensate in a light-induced vector gauge potential using 1064-nm optical-dipole-trap lasers. *Phys. Rev. A* **84**, 043609. https://doi.org/10.1103/PhysRevA.84.043609 (2011).
56. Chen, H. R. *et al.* Spin–Orbital-angular-momentum coupled Bose–Einstein condensates. *Phys. Rev. Lett.* **121**, 113204. https://doi.org/10.1103/PhysRevLett.121.113204 (2018). arXiv:1803.07860.
57. Wu, Z. *et al.* Realization of two-dimensional spin–orbit coupling for Bose–Einstein condensates. *Science* **354**, 83–88. https://doi.org/10.1126/science.aaf6689 (2016).
58. Campbell, D. L., Juzeliunas, G. & Spielman, I. B. Realistic Rashba and Dresselhaus spin–orbit coupling for neutral atoms. *Phys. Rev. A* **84**, 1–4. https://doi.org/10.1103/PhysRevA.84.025602 (2011).
59. Anderson, B. M., Juzeliūnas, G., Galitski, V. M. & Spielman, I. B. Synthetic 3d spin–orbit coupling. *Phys. Rev. Lett.* **108**, 235301. https://doi.org/10.1103/PhysRevLett.108.235301 (2012).
60. Wang, Z.-Y. *et al.* Realization of an ideal Weyl semimetal band in a quantum gas with 3D spin–orbit coupling. *Science* **372**, 271–276. https://doi.org/10.1126/science.abc0105 (2021).

61. Stanescu, T. D., Anderson, B. & Galitski, V. Spin–orbit coupled Bose–Einstein condensates. *Phys. Rev. A* **78**, 1–10. https://doi.org/10.1103/PhysRevA.78.023616 (2008).
62. Wang, C., Gao, C., Jian, C. M. & Zhai, H. Spin–orbit coupled spinor Bose–Einstein condensates. *Phys. Rev. Lett.* **105**, 1–4. https://doi.org/10.1103/PhysRevLett.105.160403 (2010).
63. Li, J. R. *et al.* A stripe phase with supersolid properties in spin–orbit-coupled Bose–Einstein condensates. *Nature* **543**, 91. https://doi.org/10.1038/nature21431 (2017).
64. Campbell, D. L. *et al.* Magnetic phases of spin-1 spin–orbit-coupled Bose gases. *Nat. Commun.* **7**, 10897. https://doi.org/10.1038/ncomms10897 (2016).
65. Dalibard, J., Gerbier, F., Juzeliūnas, G. & Öhberg, P. Colloquium: Artificial gauge potentials for neutral atoms. *Rev. Mod. Phys.* **83**, 1523–1543. https://doi.org/10.1103/RevModPhys.83.1523 (2011).
66. Galitski, V. & Spielman, I. B. Spin–orbit coupling in quantum gases. *Nature* **494**, 49–54. https://doi.org/10.1038/nature11841 (2013).
67. Zhang, S., Cole, W. S., Paramekanti, A. & Trivedi, N. Spin–orbit coupling in optical lattices. *Ann. Rev. Cold Atoms Mol.* **3**, 135–179. https://doi.org/10.1142/9789814667746_0003 (2015).
68. Zhai, H. Degenerate quantum gases with spin–orbit coupling: a review. *Rep. Prog. Phys.* **78**, 026001. https://doi.org/10.1088/0034-4885/78/2/026001 (2015).
69. Zhang, Y., Mossman, M. E., Busch, T., Engels, P. & Zhang, C. Properties of spin–orbit-coupled Bose–Einstein condensates. *Front. Phys.* **11**, 118103. https://doi.org/10.1007/s11467-016-0560-y (2016).
70. Giannozzi, P. *et al.* QUANTUM ESPRESSO: a modular and open-source software project for quantum simulations of materials. *J. Phys.: Condens. Matter* **21**, 395502. https://doi.org/10.1088/0953-8984/21/39/395502 (2009).
71. Giannozzi, P. *et al.* Advanced capabilities for materials modelling with quantum ESPRESSO. *J. Phys.: Condens. Matter* **29**, 465901. https://doi.org/10.1088/1361-648x/aa8f79 (2017).
72. Perdew, J. P., Burke, K. & Ernzerhof, M. Generalized gradient approximation made simple. *Phys. Rev. Lett.* **77**, 3865–3868. https://doi.org/10.1103/PhysRevLett.77.3865 (1996).
73. Perdew, J. P., Burke, K. & Ernzerhof, M. Generalized gradient approximation made simple [phys. rev. lett. 77, 3865 (1996)]. *Phys. Rev. Lett.***78**, 1396–1396, https://doi.org/10.1103/PhysRevLett.78.1396 (1997).
74. Monkhorst, H. J. & Pack, J. D. Special points for Brillouin-zone integrations. *Phys. Rev. B* **13**, 5188–5192. https://doi.org/10.1103/PhysRevB.13.5188 (1976).
75. Bengtsson, L. Dipole correction for surface supercell calculations. *Phys. Rev. B*https://doi.org/10.1103/PhysRevB.59.12301 *(1999).*

Acknowledgements

This work was supported by in part by PAAD Infrastructure co-financed by Operational Programme Innovative Economy, Objective 2.3, by the Interdisciplinary Centre for Mathematical and Computational Modelling (ICM), University of Warsaw (UW), within grant no. G83-27. M.K. acknowledges the support from the National Science Centre under the contract DEC-2018/29/B/ST3/01892. The project is co-financed by the Polish National Agency for Academic Exchange.

Author contributions

P.J. performed first principles calculations and post-processing of the results. M.K. formulated the problem, lead the research and performed cross-checking calculations. All authors discussed the results and wrote the manuscript.

Competing interests

The authors declare no competing interests.

Additional information

Supplementary Information The online version contains supplementary material available at https://doi.org/10.1038/s41598-022-07215-2.

Correspondence and requests for materials should be addressed to M.K.

Reprints and permissions information is available at www.nature.com/reprints.

Publisher's note Springer Nature remains neutral with regard to jurisdictional claims in published maps and institutional affiliations.